RESEARCH ARTICLE

ADVANCED
ENERGY & SUSTAINABILITY
RESEARCH
Open Access
www.advenergysustres.com

Deep Eutectic Solvents as Nonflammable Electrolytes for Durable Sodium-Ion Batteries

Dries De Sloovere, Danny E. P. Vanpoucke, Andreas Paulus, Bjorn Joos, Lavinia Calvi,
Thomas Vranken, Gunter Reekmans, Peter Adriaensens, Nicolas Eshraghi,
Abdelfattah Mahmoud, Frédéric Boschini, Mohammadhosein Safari,
Marlies K. Van Bael, and An Hardy**

Sodium-ion batteries are alternatives for lithium-ion batteries in applications where cost-effectiveness is of primary concern, such as stationary energy storage. The stability of sodium-ion batteries is limited by the current generation of electrolytes, particularly at higher temperatures. Therefore, the search for an electrolyte which is stable at these temperatures is of utmost importance. Here, such electrolytes are introduced in the form of nonflammable deep eutectic solvents (DESs), consisting of sodium bis(trifluoromethane)sulfonimide (NaTFSI) dissolved in N-methyl acetamide (NMA). Increasing the NaTFSI concentration replaces NMA—NMA hydrogen bonds with strong ionic interactions between NMA, Na^+, and $TFSI^-$. These interactions lower NMA's highest occupied molecular orbital (HOMO) energy level compared with that of $TFSI^-$, leading to an increased anodic stability (up to ≈4.65 V versus Na^+/Na). $(Na_3V_2(PO_4)_2F_3$/carbon nanotube [CNT])/$(Na_{2+x}Ti_4O_9$/C) full cells show 97.0% capacity retention after 250 cycles at 0.2 C and 55 °C. This is considerably higher than for $(Na_3V_2(PO_4)_2F_3$/CNT)/$(Na_{2+x}Ti_4O_9$/C) full cells containing a conventional electrolyte. According to the electrochemical impedance analysis, the improved electrochemical stability is linked to the formation of more robust surface films at the electrode/electrolyte interface. The improved durability and safety highlight that DESs can be viable electrolyte alternatives for sodium-ion batteries.

1. Introduction

While lithium-ion batteries (LIBs) are an established technology for portable electronics, the increased demand for lithium due to applications in large-scale energy storage, together with its limited reserves, can be expected to drive up prices.[1–3] This contrasts with the factor of low cost, which together with sustainability is key in the large-scale storage of renewable energy.[1,3–6] Sodium-ion batteries (SIBs) are an alternative to LIBs, as sodium is the lightest and smallest alkali metal after lithium. Sodium is more abundant (the Earth's crust contains 23 600 ppm sodium vs. 20 ppm lithium) and widely available, making its use more cost-effective and sustainable.[1,7] Therefore, SIBs would be a good alternative for LIBs in applications where cost and sustainability are the most crucial requirements.[4]

A viable electrolyte should be characterized by sufficient ionic conductivity, an electronically insulating nature, and a large electrochemical stability window (a large difference between the onset potentials of electrolyte reduction and oxidation). It should not react with the other components present in the battery (such as the positive and negative electrodes). Also, it should have a large thermal

D. De Sloovere, D. E. P. Vanpoucke, A. Paulus, B. Joos, L. Calvi, T. Vranken,
G. Reekmans, P. Adriaensens, M. Safari, M. K. Van Bael, A. Hardy
Institute for Materials Research (IMO-Imomec)
UHasselt and Imec
Agoralaan, building D, B-3590, Belgium
E-mail: dries.desloovere@uhasselt.be; an.hardy@uhasselt.be

The ORCID identification number(s) for the author(s) of this article can be found under https://doi.org/10.1002/aesr.202100159.

D. De Sloovere, A. Paulus, B. Joos, T. Vranken, M. Safari, M. K. Van Bael,
A. Hardy
EnergyVille
Thor Park 8320, B-3600 Genk, Belgium

N. Eshraghi, A. Mahmoud, F. Boschini
CESAM Research unit
Department of Chemistry
GREENMAT
University of Liège
Allée du Six Août, 13, B-4000 Liège, Belgium

N. Eshraghi
Center for Low-Emission Transport
Electric vehicle technologies
Austrian Institute of Technology GmbH
Giefinggasse 4, 1210 Vienna, Austria

ADVANCED
SCIENCE NEWS

www.advancedsciencenews.com

ADVANCED
ENERGY & SUSTAINABILITY
RESEARCH
Open Access

www.advenergysustres.com

stability window and should be safe, nontoxic, and inexpensive.[4,5] These characteristics should be optimized with the specific application of the battery in mind, as this also determines the operating temperature, which has a significant influence on the electrolyte's conductivity and stability. Typical liquid electrolytes for SIBs consist of sodium salts (such as NaClO$_4$, NaPF$_6$, NaBF$_4$, sodium bis(fluorosulfonyl)imide (NaFSI) or sodium bis(trifluoromethane)sulfonimide (NaTFSI)) dissolved in a solvent or in a mixture of solvents. In the category of organic solvents, carbonate esters and ethers are most often used. The high flammability of these components poses severe safety hazards. In liquid electrolytes with very high salt concentrations, there is an increased interaction between cations, anions, and solvent molecules to the extent that there are no uncoordinated solvent molecules. Such a highly concentrated electrolyte has a distinct 3D coordination structure.[8] The degradation layers formed from such concentrated electrolytes on the electrodes were reported to be mainly salt-derived, kinetically mitigating further decomposition of the salt anion and solvent.[9,10] A robust and passivating salt-derived solid−electrolyte interphase (SEI) is beneficial for battery durability, offering long-term stability of operation.[8,11–17] In addition, the electrolyte's oxidative stability can be improved because of the donation of solvent lone electron pairs to the salt cation.[18] For instance, increasing the LiTFSI concentration was shown to enhance the oxidative stability from 4 V versus Li$^+$/Li to ≈5 V versus Li$^+$/Li for both [Li(triethylene glycol dimethyl ether)] [TFSI] and [Li(tetraethylene glycol dimethyl ether)] [TFSI].[18] This was attributed to the lowering of the solvent's highest occupied molecular orbital (HOMO) energy level.

As alternatives to organic solvents, ionic liquids (ILs) are defined as materials which consist entirely of ions and remain liquid in a wide temperature range, have a high thermal and (electro)chemical stability, and are nonflammable. Furthermore, they can dissolve high amounts of salt and have a high intrinsic ionic conductivity. While ILs can be very versatile, they are often expensive due to the difficulty of their synthesis.[19] Closely related to—but inherently different from—ILs is the concept of deep eutectic solvents (DESs). A DES consists of a mixture of Lewis/Brönsted acids and bases, where the melting temperature of the mixture is below that of the individual components.[19] DESs and ILs can have similar physical properties, such as a low vapor pressure and nonflammability. However, the former can offer additional advantages such as ease of preparation, wide availability of reagents, and cost-effectiveness, although this depends on the exact composition. DESs have not yet been reported as electrolytes for SIBs. In LIBs, a DES consisting of LiTFSI in N-methyl acetamide (NMA) allowed for efficient cycling of LiFePO$_4$/Li$_4$Ti$_5$O$_{12}$ full cells with high coulombic efficiencies even at 60 °C.[20] These results inspired us to

develop a DES for SIBs. Sodium's milder Lewis acidity and the low solubility of sodium salts compared with their lithium counterparts imply that exchanging NaTFSI for LiTFSI has a significant impact on the DES's physicochemical and electrochemical properties.[2,15]

Here, we report a series of DESs as electrolytes for SIBs, based on the dissolution of NaTFSI in NMA. Increasing the concentration of NaTFSI in NMA resulted in a decreased reactivity with sodium metal, a lower flammability, and a broader electrochemical stability window, but also decreased the ionic conductivity of the electrolyte. These effects could be traced back to the replacement of NMA—NMA hydrogen bonds with strong ionic interactions, lowering NMA's relative HOMO energy level as the NaTFSI

concentration is increased, as is indicated by the electronic structure calculations of gas-phase molecules and clusters. (Na$_3$V$_2$(PO$_4$)$_2$F$_3$/carbon nanotube [CNT])/(Na$_{2+x}$Ti$_4$O$_9$/C) full cells with DES electrolyte demonstrated a considerably higher durability than cells containing a conventional organic solvent-based electrolyte. As such, the proposed set of DESs forms a new class of electrolytes for application in SIBs, which can offer a more durable electrochemical performance than conventional systems.

2. Results and Discussion

Three DES electrolytes were prepared, each with a different NaTFSI concentration. The exact compositions, along with their anodic stability limit and conductivity at 20 and 55 °C (vide infra), are summarized in **Table 1**.

2.1. Enhanced Electrolyte Stability Window and Solution Structure

As determined with linear sweep voltammetry (LSV), the onset potential of electrolyte oxidation increases with NaTFSI concentration (**Figure 1**). The anodic stability limit is ≈4.65 V versus Na$^+$/Na for 5.86 m NaTFSI/NMA and ≈4.20 V versus Na$^+$/Na for 3.42 m NaTFSI/NMA, as can be inferred from the exponential current increase caused by excessive electrolyte oxidation. Compared with the more concentrated DESs, the three-electrode cell's open-circuit potential is considerably lower when 1.52 m NaTFSI/NMA is used as the electrolyte. Furthermore, this DES has a poor anodic stability and the current response is irregular. The latter may be caused by the DES's spontaneous reaction with the Na reference and counter electrodes. To verify this assumption, we investigated the stability of the DES electrolyte with sodium by adding small amounts of sodium metal (20 mg)

Table 1. Molality, molarity (molar amount of sodium salt divided by the volume of the entire solution), molar ratio, anodic stability limit, density, and ionic conductivity at 20 and 55 °C of the electrolytes presented in this article.

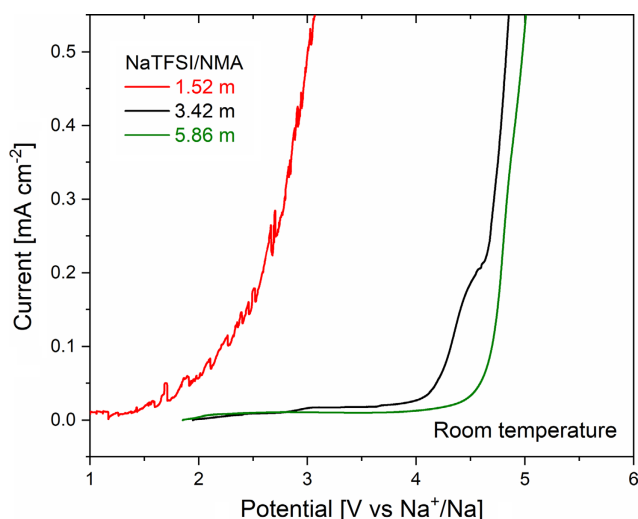| Molality [m]	Molarity [M]	[NaTFSI]/[NMA]	Anodic stability limit versus Na$^+$/Na [V]	Density at 20 °C [g ml^{-1}]	Ionic conductivity at 20 °C [mS cm^{-1}]	Ionic conductivity at 55 °C [mS cm^{-1}]
1.52	1.41	1/9	–	1.167	3.05	10.6
3.42	2.12	2/8	≈4.20	1.262	1.54	8.39
5.86	2.87	3/7	≈4.65	1.359	0.355	3.78

Figure 1. The anodic stability limit of the DES electrolytes increases with increasing NaTFSI concentration. Linear sweep voltammograms of the DESs in a three-electrode cell at a scan rate of $10\,mV\,s^{-1}$ at room temperature. The low open-circuit potential and irregular current response of the cell containing 1.52 m NaTFSI/NMA is likely related to its reactivity with the sodium counter and reference electrodes.

to the electrolytes (1 mL) and tracking their dissolution (supplementary information (SI), Figure S1). One week after addition to 1.52 m NaTFSI/NMA, the sodium metal was completely dissolved. In the more concentrated electrolytes, the sodium metal was considerably less soluble as it did not dissolve in the same time period. NMA molecules can either form hydrogen bridges with other NMA molecules, or they can form an ionic bond with a Na^+ ion through their carbonyl group, where the latter is more common in more concentrated electrolytes (vide infra). The drastically reduced reactivity of NMA with sodium metal at high NaTFSI concentrations indicates that the reactivity of NMA involved in an ionic bond is considerably lower than that of a hydrogen-bonded NMA molecule.

Previous studies on highly concentrated electrolytes traced the cause of the considerable increase in anodic stability with higher salt concentrations back to the solutions' coordination structure, where the donation of solvent lone electron pairs to the salt cation increased the electrolyte's stability against oxidation.[9,18,21] Therefore, we investigated the interactions between Na^+, $TFSI^-$, and NMA in the DESs using first-principles atomistic models, focusing on the DESs' stability, charge transfer, and electronic structure.

The structures of gas-phase clusters consisting of one NaTFSI molecule and up to four NMA molecules (SI, Figure S4) were optimized based on prior optimization of the structure of NaTFSI binding to one NMA molecule (SI, Figure S2, S3). Up to three NMA molecules form ionic bonds to Na^+, with further NMA molecules binding through hydrogen bridges to the $TFSI^-$ anion and the Na^+-bound NMA molecules (SI, Table S3). Apart from gas-phase structure optimization, clusters of NaTFSI with two, three, and four NMA molecules were optimized into forming condensed-phase molecular crystals, as examples of possible experimental configurations in the liquid

phase. One may compare this approach to taking two sample images from a molecular dynamics (MD) track, as previously reported.[9] The two optimization strategies lead to significantly different structures (SI, Table S2), with comparable formation energies. In each case, and irrespective of the number of NMA molecules, Na^+ forms five ionic bonds, two of which with the $TFSI^-$ anion. In addition, each NMA molecule can form a single ionic bond with Na^+ through its carbonyl group. In the system with only two NMA molecules (**Figure 2**a), the fifth ionic bond is formed with a third $TFSI^-$ O atom, seen as a periodic copy. A hydrogen bond is formed between the NMA NH moiety and the TFSI sulfone moiety. In the systems containing more NMA molecules, additional hydrogen bonds are formed: three or more hydrogen bonds are formed in the systems with three (Figure 2b) and four NMA molecules (Figure 2c). Once the number of NMA molecules becomes sufficiently large, the NMA molecules also form hydrogen bonds with other NMA molecules, giving rise to structures resembling solid NMA. In systems containing a low number of NMA molecules, that is, with a high NaTFSI concentration, the hydrogen bonds between NMA molecules are replaced with ionic interactions with Na^+ (as schematically shown in Figure 2d). As such, we expect Na^+ to have a lower mobility in a mixture with a high NaTFSI concentration.

Hirshfeld-I atomic charges were calculated for both gas-phase (SI, Table S4) and condensed-phase (SI, Table S5) systems.[22–24] For both cases, the Na and N (of TFSI) atomic charges remain fixed irrespective of the number of coordinated NMA molecules. This implies that despite the variation in coordination, the ionic environment of Na is very stable and that the covalent bonding remains unchanged for N.

The electronic structure for the different systems was calculated using the HSE06 hybrid functional, as it is optimized to deal with condensed-phase materials and is known to provide excellent estimates of the HOMO−lowest unoccupied molecular orbital (LUMO) gap in molecular-based systems (SI, Figure S5–S7).[25,26] The electronic band structure around the HOMO−LUMO gap for the gas-phase molecules and clusters is shown in Figure 2e. In this figure, the HOMO energy is aligned with the Fermi energy level for each case due to the lack of an external reference energy level. Still, this approach allows us to compare the HOMO−LUMO gaps of the different systems. The HOMO−LUMO gap changes with the number of involved NMA molecules, where systems with fewer NMA molecules (i.e., a higher NaTFSI concentration) have a larger HOMO−LUMO gap. The bandgaps for gas-phase NMA and NaTFSI are nearly equal. There is an increase in density of states (DOS) at the top of the HOMO band with increasing number of NMA molecules. The HOMO band structure of NaTFSI with and without one molecule of NMA is nearly identical, owing to the >2 eV gap below the NMA HOMO. To understand better what is happening in the top of this HOMO band, we investigated the atom-projected character of the molecular states (SI, Table S7). At low NaTFSI concentration (i.e., with a high number of NMA molecules), the HOMO states of $TFSI^-$ are located more than 1 eV below the HOMO of the cluster. The latter relates to the NMA oxygen and nitrogen atoms, where the presence of the N−H bond makes the nitrogen atom more likely to undergo electrochemical reactions than the oxygen atom. The $TFSI^-$ HOMO states move upward with increasing NaTFSI

**ADVANCED
SCIENCE NEWS**
www.advancedsciencenews.com

**ADVANCED
ENERGY & SUSTAINABILITY
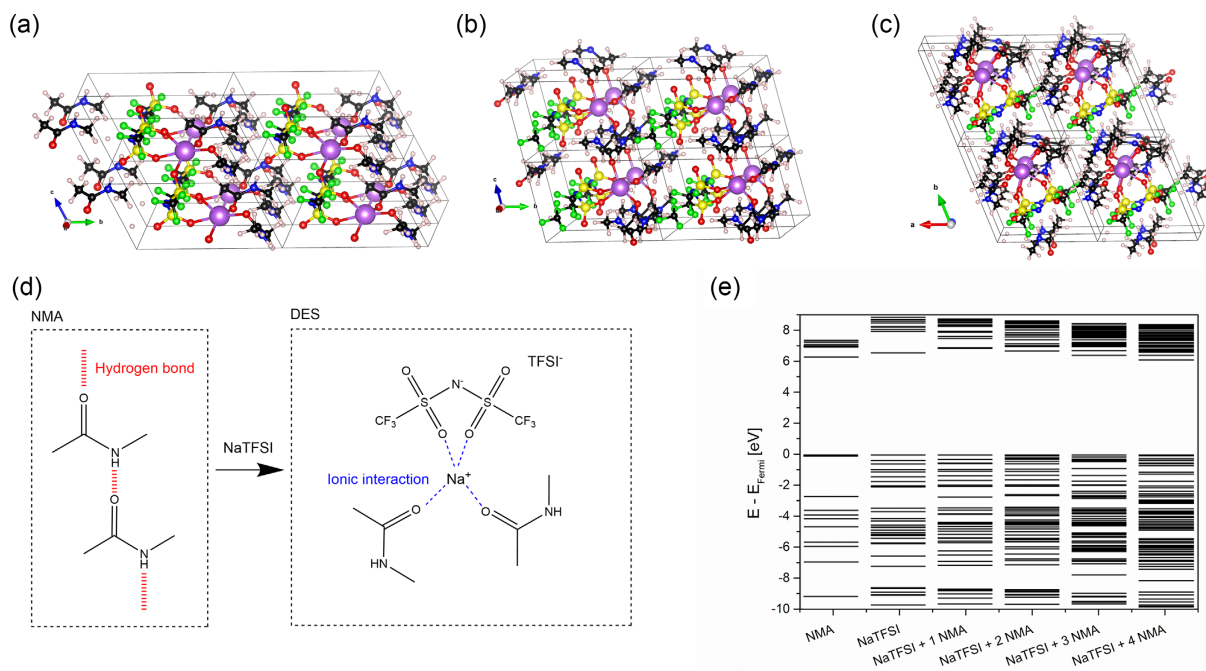RESEARCH**
Open Access
www.advenergysustres.com

Figure 2. First-principles modeling indicates that increasing the NaTFSI concentration in NMA leads to a decrease in the extent of hydrogen bonding and to an increase in the HOMO−LUMO gap. Ball-and-stick representation of the condensed-phases with a) two, b) three, and c) four NMA molecules, using the first condensation strategy and PBE + D3 functional. Unit cells are indicated by the boxes. Purple: sodium; blue: nitrogen; yellow: sulfur; red: oxygen; black: carbon; green: fluorine; white: hydrogen. d) Schematic representation of the replacement of intermolecular hydrogen bonds between NMA molecules by ionic interactions in DESs due to the addition of NaTFSI. e) Electronic band structure (HSE06 + D3) of gas-phase molecules and clusters around the HOMO−LUMO gap. The HOMO is aligned to zero for all systems.

concentration to form the HOMO for the cluster consisting NaTFSI and two NMA molecules. Here, the HOMO state mainly relates to the TFSI⁻ oxygen atom which binds to the sodium ion. The states originating from the NMA nitrogen atom are located ≈0.3 eV underneath the Fermi level and are therefore considerably less reactive than in DESs with lower NaTFSI concentration. The strong interaction of the TFSI⁻ oxygen atom with the sodium ion implies that it has a lower reactivity than in the more diluted systems. In other words, an increase in NaTFSI concentration lowers the reactivity of both NMA and TFSI⁻, resulting in a general increase in electrochemical stability. The DOS and atom-projected DOS (PDOS) present similar behavior in the condensed-phase systems (SI, Figure S8). In each case, the HOMO is formed by the states of the NMA molecules, with the NaTFSI HOMO states located below. In contrast to the gas-phase system, here also, the HOMO of the system with only two NMA molecules is formed by the states of the NMA molecules. It should be noted that in the condensed phase, an additional bond to Na^+ is formed by a periodic copy of the TFSI⁻ ion, which probably results in a lowering of the NaTFSI HOMO states. The LUMO consists of contributions of both NaTFSI and NMA, where the specific details depend on the specific local geometry. In most cases, however, the main contribution to the LUMO states comes from the NMA molecules.

As the DESs discussed in the article at hand are liquid, we assume that the condensed-phase provides a more relevant image than the gas-phase system. Despite their differences, both gas-phase and condensed-phase results clearly show that the

HOMO of the NaTFSI complex is located well below the system HOMO once a sufficient number of NMA molecules is present within a certain range. In contrast, increasing the NaTFSI concentration (i.e., decreasing the number of NMA molecules in the system) can be considered to lower the HOMO energy of the solvent relative to that of NaTFSI, which may enhance the oxidative stability. This corroborates the increase of the DESs' anodic stability limit with increasing NaTFSI concentration (Figure 1) and agrees with what was previously observed in a LiTFSI-based system.[18]

The Raman and nuclear magnetic resonance (NMR) spectroscopy results confirm the results of the quantum mechanical atomistic simulations, which predicted that the hydrogen bonds between NMA molecules are progressively disrupted when the NaTFSI concentration increases. A complete Raman peak assignment of NMA and DESs is given in the SI, Table S8 (**Figure 3**a).[27–30] The amide A band at 3300 cm⁻¹ in the NMA spectrum corresponds to the stretching of hydrogen bonded N−H groups (Figure 3b). In the DES spectra, there is an additional band at 3419 cm⁻¹, which can be mainly attributed to N−H groups not involved in hydrogen bonding. This indicates that a fraction of the hydrogen bonds is replaced by ionic interactions. The former band disappears for 5.86 m NaTFSI/NMA, indicating that a large number of hydrogen bonds is broken in favor of ionic interactions. This is in line with the structural results of the condensed-phase calculations, showing a drastic reduction in the amount of hydrogen bonds as the number of NMA molecules in the system decreases (i.e., when the NaTFSI concentration increases). The amide I band shifts to higher wave numbers with increasing NaTFSI concentration.
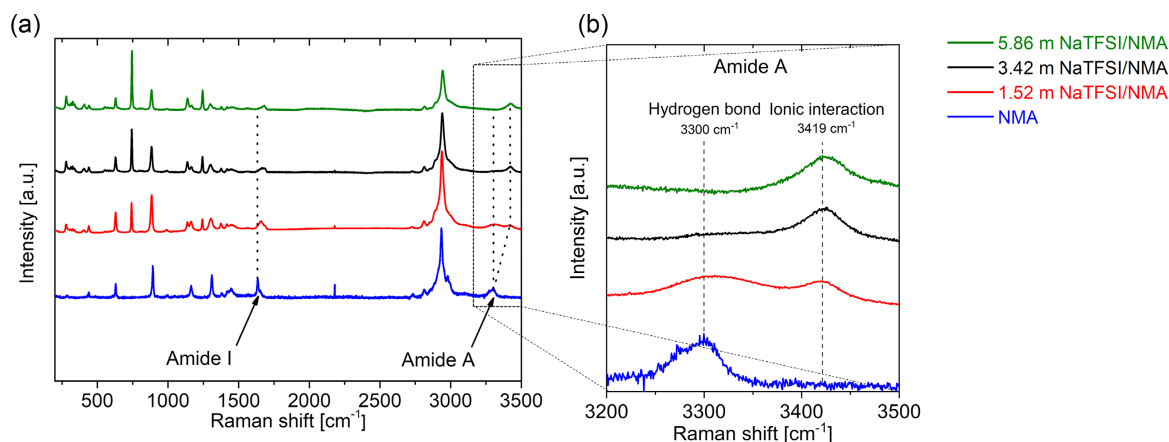
Figure 3. An increased salt concentration replaces NMA—NMA hydrogen bonds by ionic interactions between NMA, Na$^+$, and TFSI$^-$. a,b) Raman spectra of NMA and the DESs with increasing NaTFSI concentration.

The replacement of hydrogen bonds by ionic interactions with increasing NaTFSI concentration was further confirmed by NMR spectroscopy (**Figure 4**). In ^{1}H NMR, intermolecular hydrogen bonding typically causes a downfield shift of the NMR signal. The DES ^{1}H NMR spectra (Figure 4a) show a pronounced upfield shift of the NH signal of NMA from around 7.4 to 6.5 ppm with increasing salt concentration, indicating that the extent of hydrogen bonding decreases with increasing NaTFSI concentration. A less pronounced upfield shift is observed for NMA's CH$_3$—C=O methyl group singlet from around 2.6 to 2.3 ppm and for the NH—CH$_3$ methyl group doublet from around 1.8 to 1.5 ppm.

Also in the ^{19}F NMR spectra (Figure 4b), the CF$_3$ signal shifts to lower ppm values with increasing NaTFSI concentration, indicating that the TFSI$^-$ ions participate in the ionic interactions. In addition, the ^{23}Na NMR spectra (Figure 4c) show that higher NaTFSI concentrations in NMA lead to an upfield shift with increasing salt concentration and severe signal broadening. This indicates that also the Na$^+$ ions play an active role in the ionic interactions, which is in line with the results from our structural modeling as well as the calculated atomic charges. The broadening of the signal suggests that this interaction also leads to a reduced freedom of mobility of the Na$^+$ ion and
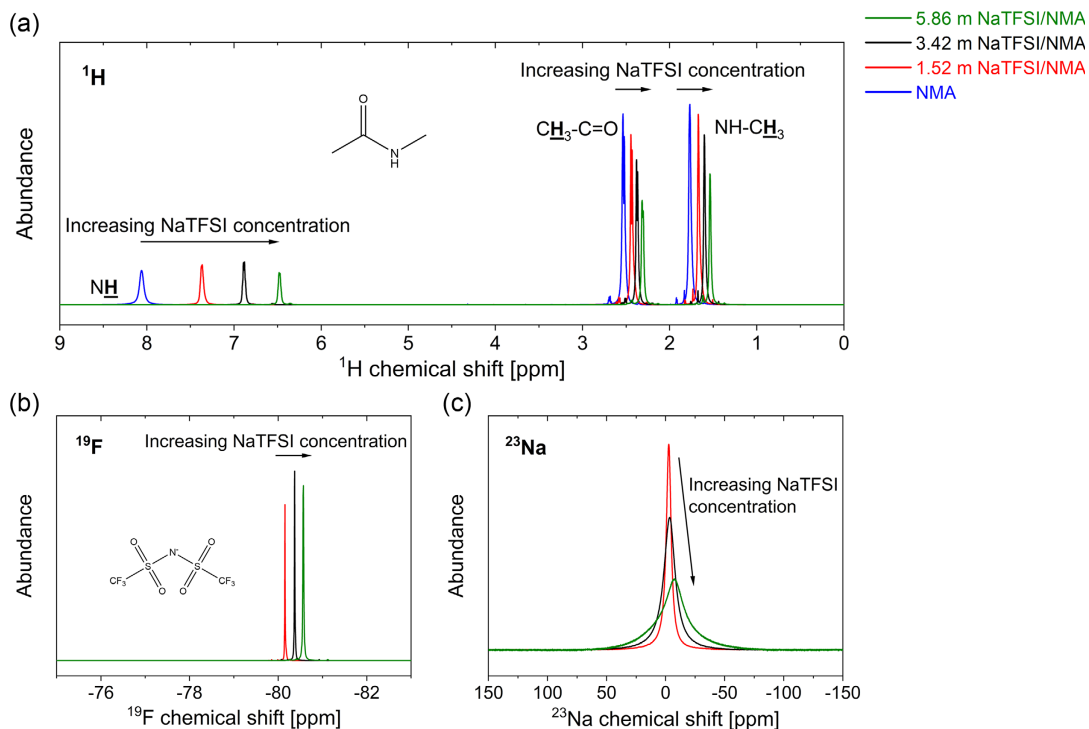

Figure 4. Increasing the NaTFSI concentration leads to upfield shifts of the NMR signals and broadening of the ^{23}Na NMR signal, indicating a decreased extent of hydrogen bonding and a reduced Na$^+$ mobility. a) ^{1}H, b) ^{19}F, and c) ^{23}Na NMR spectra of NMA (only ^{1}H spectrum) and the DESs.
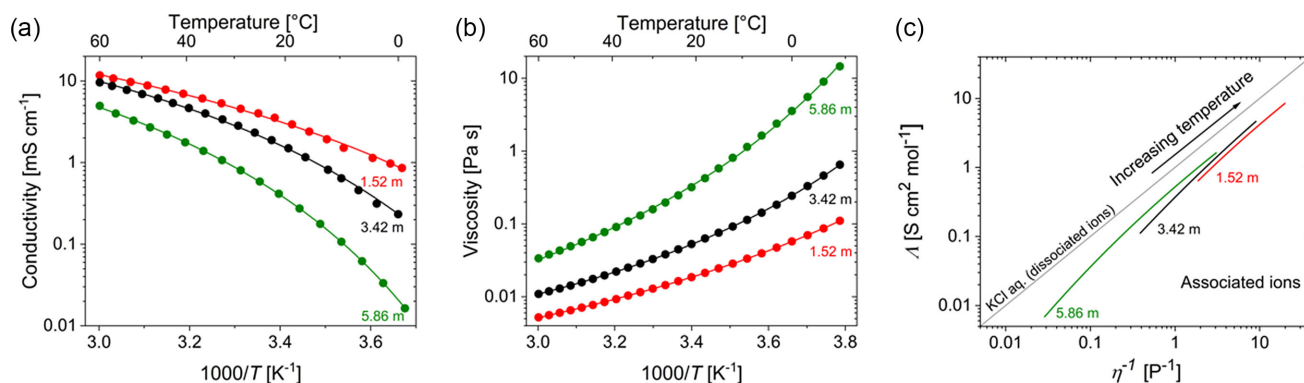
Figure 5. The ionic conductivity decreases and viscosity increases, with increasing salt concentration. Arrhenius plots of the a) ionic conductivity, b) viscosity, and c) Walden plot of the NaTFSI/NMA solutions.[35–37] Data points are represented by dots, whereas the full lines represent the fits to the VTF equation.

therefore to a decreased conductivity. This latter aspect we can understand from the structural calculations, which indicate that for higher NaTFSI concentrations, the Na$^+$ cation forms three ionic bonds with TFSI$^-$ anions, which were calculated to be stronger than the ionic bonds between the Na$^+$ cation and the NMA carbonyl group.

2.2. Conductivity and Viscosity

The conductivity and viscosity of every electrolyte was measured as a function of temperature (in the range of −9–60 °C) (**Figure 5**). Across the whole investigated temperature range, more concentrated DESs have a higher viscosity and a lower conductivity. This was already indicated by our condensed-phase models and NMR spectroscopy results, showing a decrease in hydrogen bonds in favor of an increase in ionic bonding. For all three solutions, the variation of both the ionic conductivity and viscosity with temperature could be fit to the Vogel−Tammann−Fulcher (VTF) equation,[31–33] as was previously reported for DES electrolytes for LIBs.[20]

$$\sigma = \sigma_0 e^{\frac{-B}{T-T_0}}$$ (1)

and

$$\eta = \eta_0 e^{\frac{B'}{T-T_0}}$$ (2)

In these equations, the pre-exponential factors σ_0 and η_0 are the conductivity and viscosity, respectively, at infinite temperature. The pseudoactivation energies (B, B') together with the

Vogel temperature T_0 describe the temperature dependence. The values of the fitted parameters are given in **Table 2**. They can be used to interpolate the conductivity and viscosity of the different electrolytes within the investigated temperature range but cannot accurately describe the solutions' physical properties outside this range.

The 1.52 m NaTFSI/NMA solution has a conductivity of 3.05 mS cm^{-1} at 20 °C, which increases to 10.6 mS cm^{-1} at 55 °C. The 3.42 m NaTFSI/NMA solution has a conductivity of 1.54 and 8.39 mS cm^{-1} at these respective temperatures. At 20 °C, the most concentrated DES (5.86 m NaTFSI/NMA) has a rather low conductivity of 0.355 mS cm^{-1}, which increases to 3.78 mS cm^{-1} at 55 °C.

A solution's ionic conductivity (σ) is determined on the one hand by the solvation/dissociation of ionic species and on the other hand by the mobility of these species.[34] The ionic conductivity is directly and inversely proportional to the solution's ionicity (or the extent of dissociation) and viscosity, respectively (SI, Equation S(1)–(3)).[35] This is for instance the case for diluted aqueous KCl solutions, where the ions are completely dissociated and have equal mobility.[35–37] Such an ideal behavior is represented by a straight line which runs through the origin in a Walden plot. The latter shows the correlation between the solution's molar conductivity (Λ (S cm^2 mol^{-1}), the ionic conductivity divided by the molar concentration), and its reciprocal viscosity (η^{-1} (P^{-1})) with logarithmic scales. There is a downward deviation from the linear ideal trend when the ion dissociation in the electrolyte is incomplete.[35–37] The Walden plot for our DES electrolytes is shown in Figure 5c. For all three electrolytes, the deviation from ideal behavior is the largest at the lowest

Table 2. Parameters of the VTF equation fit to the data of conductivity and viscosity as a function of temperature for the NaTFSI/NMA solutions.

	Conductivity			Viscosity		
	σ_0 [mS cm^{-1}]	B [K]	T_0 [K]	η_0 [mPa s]	B' [K]	T_0 [K]
1.52 m NaTFSI/NMA	319	447	197	0.118	582	178
3.42 m NaTFSI/NMA	389	438	214	0.252	500	201
5.86 m NaTFSI/NMA	378	475	225	0.150	695	204

**ADVANCED
SCIENCE NEWS**

www.advancedsciencenews.com

**ADVANCED
ENERGY & SUSTAINABILITY
RESEARCH**
Open Access

www.advenergysustres.com

temperature. Increasing the temperature results in a higher degree of dissociation, as can be inferred from the smaller downward deviation from the ideal line.

The observations show that the increase in the DESs' conductivity with temperature is governed by both the decrease in viscosity and the improved ion dissociation. This might explain the observed difference in pseudoactivation energy for conductivity as compared with viscosity (Table 2).

2.3. Thermal Stability and Flammability

DSC was performed to assess the occurrence of thermal phenomena (SI, Figure S9) affecting the ionic conductivity. All DES electrolytes were liquid above −5 °C, excluding the presence of solid phases as the cause for the low conductivity of the DESs below room temperature.[38] The thermal stability of the electrolytes is limited by the evaporation of NMA (SI, Figure S10), as was previously reported for similar electrolytes.[39,40] Although the thermal stability of 1.52 m and 3.42 m NaTFSI/NMA is limited (<100 °C), 5.86 m NaTFSI/NMA is stable up to higher temperatures (≈100 °C), presumably because of the strong ionic interactions between NMA and Na⁺ and TFSI⁻ ions. This last aspect is corroborated by our condensed-phase models, presenting an additional ionic bond between the TFSI⁻ ions and two Na⁺ ions, leading to a tighter and more extended network.

The flammability of the liquid electrolyte has a profound impact on the safety of battery operation. A combustion test was performed to determine the flammability of the proposed set of DESs. A volume of 200 μl of each DES was directly exposed to a gas flame until ignition occurred (**Figure 6**). Both 1.52 and 3.42 m NaTFSI/NMA could be ignited after roughly 3−4 s of flame contact, which resulted in a short-lived (<1 s) flame with low intensity. The 5.86 m NaTFSI/NMA DES could not be ignited, and repeated flame contact only led to evaporation. The flash point of conventional organic electrolytes was reported to be determined by the flash point of the most flammable component,[41] which is NMA in this case. A sample can only be ignited if an ignitable vapor−air mixture can be formed. Pure NMA has a flash point of 108 °C and its low vapor pressure prohibits the formation of combustible vapor, which explains the difficult ignition of 1.52 and 3.42 m NaTFSI/NMA.[42] The further decrease in flammability of 5.86 m NaTFSI/NMA can be explained by the strong ionic interactions, which further decrease the vapor pressure. The flammability of electrolytes can be classified using the self-extinguishing time (SET), which

expresses the flame's lifetime normalized to the sample mass.[41] According to this classification, all proposed DESs are nonflammable as the SET is smaller than 6 s g⁻¹ for each sample.

2.4. Electrolyte Application in Full Cell Coin Cells

Given the broadened electrochemical potential window of 5.86 m NaTFSI/NMA, this electrolyte was chosen for electrochemical characterization in conjunction with active SIB electrodes as a proof of concept. At room temperature, this DES has a low ionic conductivity (0.355 mS cm⁻¹) compared with conventional electrolytes (≈8 mS cm⁻¹ for a 1 M solution of NaClO₄ in ethylene carbonate/propylene carbonate [EC/PC]).[4] This means that this DES is likely to limit the battery rate capability in these conditions, even when combined with electrodes which exhibit fast kinetics (vide infra). Therefore, the electrochemical tests were performed at 55 °C, where this DES has an ionic conductivity of 3.78 mS cm⁻¹. At this temperature, the solubility of SEI components (in addition to the occurrence of parasitic reactions) is higher than that at room temperature.[11] Furthermore, the SEI components in SIBs generally have a higher solubility than their LIB counterparts because of sodium's milder Lewis acidity. This is problematic for battery performance, as the SEI should ideally be strong, insoluble, and stable to ensure optimal electrochemical characteristics.[8,11–14] The 5.86 m NaTFSI/NMA DES may offer an improved battery performance at 55 °C because of the potential formation of robust surface films, as was previously observed for other concentrated electrolytes.[43]

Despite the improved reductive stability caused by its high concentration, the stability of 5.86 m NaTFSI/NMA is not high enough to be used in a cell with sodium metal as the negative electrode. Therefore, battery characterization tests were instead performed using a Na₂₊ₓTi₄O₉/C negative electrode and a Na₃V₂(PO₄)₂F₃/CNT (NVPF/CNT) positive electrode.[44] NVPF is electrochemically active between 2 and 4.5 V versus Na⁺/Na and has a theoretical capacity of 128 mAh g⁻¹, corresponding to the reversible extraction of two sodium ions per formula unit.[45–49] These extractions involve a range of biphasic reactions and one solid-solution reaction,[48] resulting in four redox steps (3.68, 3.70, 4.16, and 4.19 V versus Na⁺/Na) in two distinct voltage regions. These regions can be observed in the galvanostatic charge/discharge profiles of the NVPF/CNT composite (**Figure 7**a, sodium-ion half cell, 1 M NaClO₄ in EC/PC electrolyte), confirming that NVPF is the electrochemically active phase. The composite is durable (97.7% capacity retention after 100
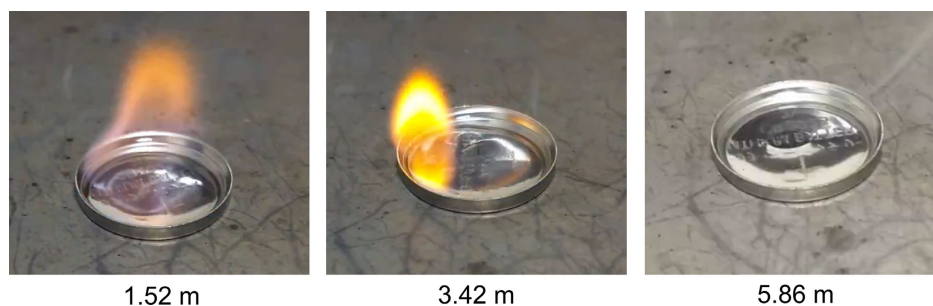

| 1.52 m | 3.42 m | 5.86 m |

Figure 6. The DESs are nonflammable and the 5.86 m NaTFSI/NMA DES cannot be ignited. Photographs of 200 μL DES directly after (attempted) ignition with a gas flame.
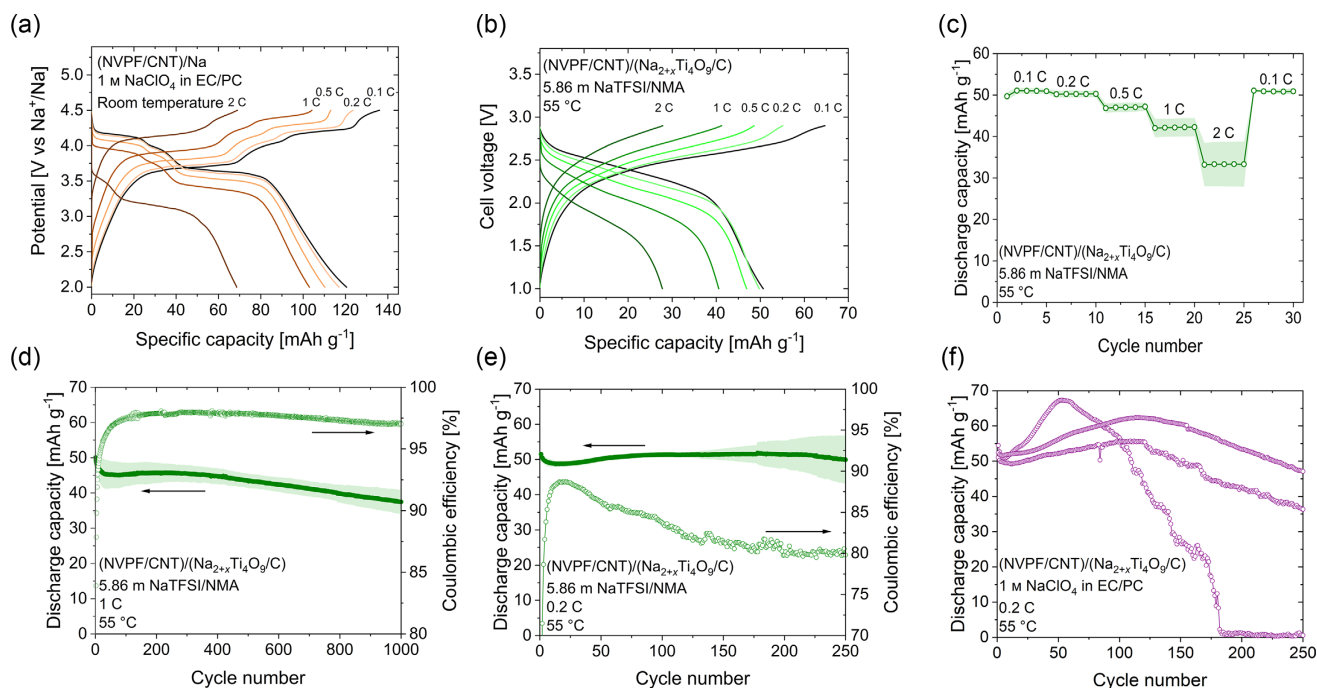
ADVANCED
SCIENCE NEWS
www.advancedsciencenews.com

ADVANCED
ENERGY & SUSTAINABILITY
RESEARCH
Open Access
www.advenergysustres.com

Figure 7. Full cells with 5.86 m NaTFSI/NMA electrolyte show an improved durability compared with organic electrolyte-based full cells. a) Galvanostatic charge/discharge profiles of (NVPF/CNT)/Na half cells containing 1 M NaClO$_4$ in EC/PC at rates from 0.1 to 2 C at room temperature. b) Galvanostatic charge/discharge profiles of (NVPF/CNT)/(Na$_{2+x}$Ti$_4$O$_9$/C) full cells containing 5.86 m NaTFSI/NMA at rates from 0.1 to 2 C at 55 °C. c) Discharge capacity of 5.86 m NaTFSI/NMA containing (NVPF/CNT)/(Na$_{2+x}$Ti$_4$O$_9$/C) full cells at rates from 0.1 to 2 C at 55 °C. d) Capacity retention and coulombic efficiency of 5.86 m NaTFSI/NMA containing (NVPF/CNT)/(Na$_{2+x}$Ti$_4$O$_9$/C) full cells at 1 C at 55 °C. e) Capacity retention and coulombic efficiency of 5.86 m NaTFSI/NMA containing (NVPF/CNT)/(Na$_{2+x}$Ti$_4$O$_9$/C) full cells at 0.2 C at 55 °C. f) Capacity retention of three similar cells with 1 M NaClO$_4$ in EC/PC containing (NVPF/CNT)/(Na$_{2+x}$Ti$_4$O$_9$/C) full cells at 0.2 C at 55 °C. Capacities were normalized to the NVPF content (positive electrode active material). The shaded areas indicate the standard deviation according to at least three measurements' repetitions.

cycles at 1 C; SI, Figure S11), which is a necessary condition to properly assess the impact of DES on the electrochemical performance of the cells. A more detailed description of the electrochemical performance of NVPF/CNT sodium-ion half cells is given in the SI (Figure S11, S12). A Na$_{2+x}$Ti$_4$O$_9$/C composite was chosen as the negative electrode because of its high durability (capacity retention of 89% after 250 cycles at 1 C).[50] This composite is electrochemically active between 0.01 and 2.5 V versus Na$^+$/Na and has slanted open-circuit potential curves. For a more detailed electrochemical description, we refer the reader to our previous work.[50]

The capacity in the highest voltage region of NVPF ($\approx$4.2 V versus Na$^+$/Na), which can be accessed in half cells containing a conventional electrolyte (Figure 7a), could not be reversibly accessed in 5.86 m NaTFSI/NMA-based cells, as was shown in exploratory experiments. This observation can be attributed to the occurrence of electrolyte degradation even below the anodic stability limit determined by LSV ($\approx$4.65 V versus Na$^+$/Na, Figure 1), which may be more pronounced because of the higher temperature and low currents during galvanostatic cycling. To avoid excessive electrolyte degradation, the upper voltage limit of the full cells was adjusted to 2.9 V, where about half of the theoretical capacity of NVPF is accessible (Figure 7b). In the voltage window of 1.0−2.9 V, the 5.86 m NaTFSI/NMA-based cells have an average capacity of 51, 50, 47, 42,

and 33 mAh g^{-1} at 0.1, 0.2, 0.5, 1, and 2 C, respectively (Figure 7c), which is comparable with similar full cells containing a conventional electrolyte (SI, Figure S13). This indicates that the rate capability of full cells at 55 °C is limited by the rate-determining processes at particle level within the electrodes (e.g., intraparticle diffusion) and not solely by the DES. After 1000 charge/discharge cycles at 1 C (Figure 7d), the 5.86 m NaTFSI/NMA-based cells retain 74.8% of their initial capacity with the coulombic efficiency reaching values of around 97−98%. The coulombic efficiency is mainly limited by DES degradation at high state of charge (SOC, SI, Figure S14). After 250 charge/discharge cycles at 0.2 C (Figure 7e), the cells retain 97.0% of their initial capacity. This capacity retention is considerably higher than that of full cells containing a conventional organic solvent-based electrolyte (Figure 7f, SI, Figure S15). In similar conditions, three cells with conventional electrolyte showed significant variations in electrochemical stability, with one cell not showing any appreciable capacity retention after less than 200 cycles. In all cases, the capacity increased over the course of the initial 100−125 cycles due to smaller polarization during charge (observed for both electrolytes; SI, Figure S16). As the NVPF voltage plateau around 4.2 V versus Na$^+$/Na is inaccessible for the full cells containing DES electrolyte, this does not lead to a significant capacity increase. However, as the conventional electrolyte has a higher anodic stability limit, the decrease
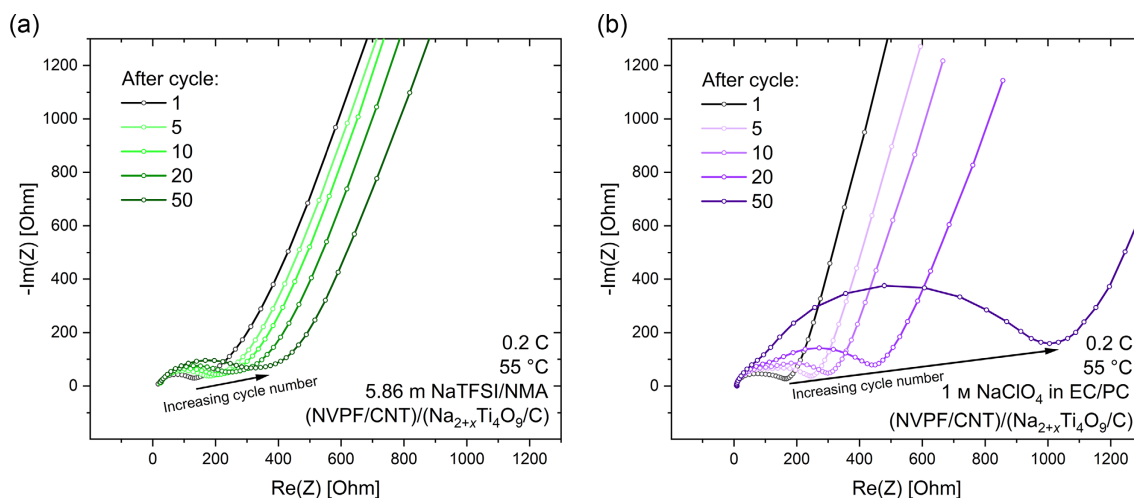
Figure 8. The surface layers formed by the electrolyte decomposition in the DES electrolyte cause a lower hindrance to the electrode kinetics compared with those when using a conventional carbonate solvent-based electrolyte. Nyquist plot representation of impedance spectra of (NVPF/CNT)/$(Na_{2+x}Ti_4O_9/C)$ cells containing a) 5.86 m NaTFSI/NMA or b) 1 M $NaClO_4$ in EC/PC after 1, 5, 10, 20, and 50 cycles at 0.2 C (with an open-circuit potential period of 2 h after every cycle). The impedance spectra were recorded over a frequency range of 10 kHz–10 mHz and subject to a potential amplitude of 10 mV.

in polarization unlocks the capacity of the higher voltage region. After the initial increase, however, the capacity decay is far more pronounced in full cells containing conventional electrolyte.

To assess the formation of surface films on the electrode/electrolyte interfaces with increasing cycle number, electrochemical impedance spectroscopy was performed after the 1st, 5th, 10th, 20th, and 50th cycles (0.2 C, after an open-circuit potential period of 2 h, **Figure 8**). In full cells containing 5.86 m NaTFSI/NMA, the charge transfer resistance (R_{ct}) increases slightly with the number of charge/discharge cycles (Figure 8a). Full cells containing conventional electrolyte, however, experience a much greater rate of increase in R_{ct} (Figure 8b). This implies that the surface films formed in 5.86 m NaTFSI/NMA are more stable and less resistant to the flow of charge compared with those in conventional electrolyte. The more beneficial character of the surface films formed by the DES may contribute to the excellent electrochemical stability, which was observed in the galvanostatic cycling experiments.

3. Conclusion

This article introduces the class of DESs as electrolytes for SIBs. The DESs, consisting of NaTFSI dissolved in NMA, are nonflammable, which has a positive impact on the safety of battery operation when compared with conventional electrolytes. We observed that NMA spontaneously reacts with sodium metal and can therefore not be used in conjunction with sodium metal as the negative electrode, even if the dissolution of large amounts of salt increases the electrolyte's reductive and oxidative stability. The increased anodic stability arises from the strong ionic interactions of NMA, Na^+, and $TFSI^-$, which lower NMA's relative HOMO energy level at high salt concentrations, as indicated by electronic structure calculations on gas-phase molecules and clusters. The most concentrated DES is stable up to

$\approx$4.65 V versus Na^+/Na and has a conductivity of 0.355 mS cm^{-1} at 20 °C and 3.78 mS cm^{-1} at 55 °C. (NVPF/CNT)/$(Na_{2+x}Ti_4O_9/C)$ full cells showed a higher electrochemical stability when DES was used in comparison with when a conventional electrolyte was used, enabling 74.8% capacity retention after 1000 cycles at 1 C and 55 °C and 97.0% capacity retention after 250 cycles at 0.2 C and 55 °C. The impedance analysis revealed a higher stability of the electrode/electrolyte interfaces for the DES compared with the conventional electrolytes.

A remaining challenge for practical use of this set of DES electrolytes is the observed trade-off between their chemical/electrochemical stability and their ionic conductivity. Further research and development (with a focus on coordination structure) are therefore essential to combine these two functional properties. As in this case, the DESs' stability was limited by the reactivity of NMA, the use of a less reactive component may allow to increase the chemical/electrochemical stability while simultaneously decreasing the required salt concentration, which would increase the ionic conductivity. Even considering the observed trade-off, the advantages of the use of DESs, as a new class of SIB electrolytes, are clear: they are nonflammable, offering an improved safety over conventional electrolytes, in addition to a longer cycle life. Compared with ILs, DESs can be more cost-effective because of the wide availability of reagents. Therefore, DESs can be viable electrolyte alternatives for SIBs.

4. Experimental Section

Preparation of the DES Electrolytes: The desired amount of sodium bis(trifluoromethane)sulfonimide (NaTFSI, Sigma Aldrich, 97%) was added to molten N–methyl acetamide (NMA, Alfa Aesar, 99%) and stirred at 80 °C until completely dissolved. The NMA was dried with molecular sieves prior to use. The operations were performed in a nitrogen-filled glovebox (MBraun, H_2O < 0.1 ppm, O_2 < 0.1 ppm). Afterward, the electrolyte solutions were stored in the glovebox at room temperature until further use.

Synthesis of $Na_3V_2(PO_4)_2F_3$/CNT: The $Na_3V_2(PO_4)_2F_3$/CNT (NVPF/CNT) composite was synthesized using a spray-drying procedure based on previous literature reports.[44] A solution of V_2O_5 (12.5 mmol, Sigma Aldrich, 98%), ammonium dihydrogen phosphate (25 mmol $NH_4H_2PO_4$, J.T. Baker, 99.9%), and ascorbic acid (12.5 mmol, $C_6H_8O_6$, Sigma Aldrich, >99%) in deionized water (800 mL) was stirred for 1 h under argon atmosphere at 80 °C. Subsequently, NaF (Alfa Aesar, 99%) was added in a 4:1 ratio of NaF to V_2O_5 in addition to 20 wt% CNT (Aquacyl AQ0302-nanocyl 3 wt%, NC7000 multiwall CNT waterborne dispersion). This dispersion was cooled down to room temperature and then spray dried in a semi-industrial spray dryer (Niro Mobile Minor, 25 mL min^{-1} feed rate, 1 bar air pressure, two-fluid nozzle injector). The material was then treated at 600 °C for 2 h (heating rate: 150 °C h^{-1}). The resulting powders were ball milled (60 min, 0.5 mm-diameter zirconia balls [BPR = 50], 250 rpm in alternate rotation mode, suspended in water). Finally, the material was dried at 70 °C for 24 h. The final carbon content in the NVPF/CNT composite was 36.5%, comprising CNT and pyrolytic carbon formed after thermal treatment of ascorbic acid.

Synthesis of $Na_{2+x}Ti_4O_9$/C: The reduced $Na_{2+x}Ti_4O_9$/C composite was synthesized as detailed in our previous work.[50] An aqueous Ti^{4+} precursor was made by adding titanium isopropoxide (3 mL, $Ti[OCH(CH_3)_2]_4$, Acros Organics, 98+%) to milli-Q water, resulting in the precipitation of hydrated titanium oxyhydroxide. This precipitate was recovered and subsequently washed with milli-Q water. A mixture of aqueous citric acid solution (3.33 mL, 3 M, $C_6H_8O_7$, Sigma-Aldrich, 99%) and H_2O_2 (1 mL, Merck, 35%) was added to the precipitate. The resulting suspension was stirred at 60 °C until the precipitate dissolved, after which ammonia (35%, NH_3, Merck) was added until the pH reached 6.5. The solution was cooled to room temperature, adjusted to pH 7 by further addition of ammonia, and diluted with water to 100 mL, resulting in a solution with a concentration of ≈0.1 M. An aqueous Na^+ precursor was made by dissolving sodium carbonate decahydrate ($Na_2CO_3 \cdot 10H_2O$, UCB, >99.0%) in water in a concentration of 1 M. This solution had a pH of 11.05. The exact concentration of both monometal precursor solutions was determined with inductively coupled plasma-atomic emission spectroscopy (ICP−AES, Optima 3300 DV, PerkinElmer). The solutions were mixed in a Na^+:Ti^{4+} ratio of 0.8:1 (resulting in a pH of 8.8). The mixed solution was dried overnight at 90 °C in a static oven. The resulting powder was ground in a mortar and thermally treated in a tube furnace at 900 °C for 2 h under argon atmosphere. The tube furnace was flushed with argon for 1 h before the thermal treatment. The heating rate was 10 °C min^{-1}. The sample was further ground in a mortar.

Physicochemical Characterization: The thermal decomposition of the electrolytes was studied by thermogravimetric analysis (TGA, TA instruments Q600), heating 6−8 mg of the samples at 10 °C min^{-1} to 600 °C under dry air flow. Calorimetric experiments were performed using a differential scanning calorimeter (DSC, TA Instruments Q200). The samples, enclosed in aluminum hermetic pans, were heated from −90 to 60 °C at 10 °C min^{-1} under a nitrogen flow of 50 mL min^{-1}. The instrument was flushed with nitrogen gas during 20 min before beginning the measurements. Raman measurements were conducted on a Horiba Jobin Yvon T64000 spectrometer, equipped with a 488 nm Lexel SHG laser operated at less than 80 mW. NMR spectra were acquired with a 5 mm Royal HFX probe at 30 °C on a Jeol ECZ400R spectrometer at 399.8, 376.2, and 105.7 MHz for ^1H, ^{19}F, and ^{23}Na spectra, respectively. ^1H spectra were collected with a 90° pulse of 6.6 μs, a spectral width of 6 kHz (15 ppm), an acquisition time of 2.2 s, a preparation delay of 12 s, and 64 scans. ^{19}F spectra were collected with a 90° pulse of 7.9 μs, a spectral width of 151.5 kHz (400 ppm), an acquisition time of 0.7 s, a preparation delay of 10 s, and 64 scans. ^{23}Na spectra were collected with a 90° pulse of 22 μs, a spectral width of 42.4 kHz (400 ppm), an acquisition time of 0.2 s, a preparation delay of 10 s, and 100 scans. The viscosity of the electrolytes was measured on a MCR102 rheometer (Anton Paar), at a shear rate of 100 s^{-1}.

Electrochemical Characterization: The electrochemical stability window of the electrolytes was determined by performing LSV measurements with a VMP3 potentiostat (Bio-Logic) from the open-circuit potential up to 5 V

versus Na^+/Na (at 10 mV s^{-1}) in a three-electrode cell (ECC-Combi, EL-CELL) with a stainless steel working electrode, a Na metal counter, and a separate Na metal reference electrode. The electrodes were separated by a glass fiber separator (18 mm by 1.55 mm thickness, EL-CELL), which was completely soaked with the electrolyte under investigation. Conductivity measurements were performed using a Mettler Toledo FiveEasy Plus conductometer, while the samples were placed in a thermostatic bath.

Electrode slurries were formulated with 80 wt% active composite material, 10 wt% carbon black (Super C65, Imerys), and 10 wt% poly (vinylidene fluoride) (PVDF, Alfa Aesar). These components were mixed in *N*-methyl-2-pyrrolidone (NMP, Alfa Aesar, 99.0%+) by ball milling (Retsch Emax, 500 rpm, 30 min, zirconia balls of 1 cm diameter). The NVPF/CNT slurry was coated on a 15 μm-thick aluminum foil (blade thickness: 150 μm). The $Na_{2+x}Ti_4O_9$/C slurry was coated on a 25 μm-thick copper foil (blade thickness: 150 μm). The coated slurries were dried at 110 °C in a vacuum oven (2 h). Punches (mass loadings of 1.42 mg cm^{-2} and 2.10 mg cm^{-2} for NVPF/CNT and $Na_{2+x}Ti_4O_9$/C, respectively) were further dried overnight under vacuum at 110 °C.

($Na_{2+x}Ti_4O_9$/C)/Na, (NVPF/CNT)/Na and (NVPF/CNT)/($Na_{2+x}Ti_4O_9$/C) coin cells (type CR2025) were assembled in an argon-filled glovebox (MBraun, H_2O < 0.1 ppm, O_2 < 0.1 ppm) using a thin glass fiber (EL-CELL, 19 mm diameter and 0.26 mm thickness) as separator, containing either a DES or a conventional electrolyte ($NaClO_4$ (1 M, Alfa Aesar, 98.0–102.0%) in EC/PC (1:1)). The $Na_{2+x}Ti_4O_9$/C electrode in full cells was first discharged (to 0.01 V versus Na^+/Na) and charged (to 2.5 V versus Na^+/Na) in half-cell configuration at 0.1 C and 55 °C (conventional electrolyte). Considering the practical capacity and mass loadings of the electrodes, the full cells were cathode limited, with a 150% anode capacity excess. After assembly, the coin cells underwent galvanostatic cycling in a BCS-805 (Bio-Logic) battery tester in the voltage window of 2−4.5 V versus Na^+/Na for half cells and 1−2.9 V for full cells. Electrochemical impedance spectra were recorded over a frequency range of 10 kHz−10 mHz (10 mV amplitude).

First-Principles Modeling: First principles, density functional theory (DFT) calculations were performed using the Vienna Ab-initio Simulation Package (VASP).[51,52] All structures were optimized using a conjugate gradient method, with the final largest forces on a single atom being below 2 meV Å^{-1}. The electron exchange correlations were described using the generalized gradient approximation (GGA) as proposed by Perdew, Burke, and Ernzerhof (PBE).[53] Van der Waals dispersive interactions were included via the D3 corrections with Becke−Johnson damping, as proposed by Grimme et al.[54,55] For the gas-phase molecules or clusters, the reciprocal space was sampled using the Gamma point only, while an extended Gamma-centered *k*-point grid was used for the solids. For all systems, the kinetic energy cutoff was set to 600 eV. To obtain highly accurate electronic structures of all our systems, we made use of the HSE06 hybrid functional,[25] with Van der Waals dispersive corrections as earlier, as this approach was well known to show excellent agreement with experimental observation for molecular crystals.[26]

All systems were placed in periodic boxes of $15 \times 15 \times 15$ Å^3, separating the molecules by about 10 Å in each direction. Larger cells of $19 \times 20 \times 15$ Å^3 were considered for convergence purposes, showing the relative energies of the individual molecules to be converged within a few meV per molecule. The atomic charges were found to be converged within less than 0.01 electron.

Atomic charges were calculated using the Hirshfeld-I method implemented in the HIVE code.[22–24] The electron density was integrated over a logarithmic radial grid combined with atom-centered Lebedev−Laikov spherical grids of 1202 grid points per shell.[56,57] The convergence criterion for the iterative scheme was set to 10^{-5} electron for each atom.

Modeling Condensed-Phase Systems (Molecular Crystals): For comparison, the molecular crystal of NMA obtained from Vasylyeva et al.[58] was optimized at the PBE + D3 level using a $3 \times 3 \times 3$ *k*-point set, while accurate electronic structures were obtained using $3 \times 3 \times 3$ (HSE06 + D3) and $5 \times 5 \times 5$ (PBE + D3) *k*-point sampling of the Brillouin zone.

Of the system at hand, no crystal structures of the molecular crystal are available in literature. To gain some insights into the non-gas-phase

behavior of the system, we generated molecular crystals by allowing the structure optimization algorithm to optimize the volume of initially gas-phase systems as well. One could consider this an algorithmic simplified equivalent to condensation of gas-phase clusters. Although it is unlikely that the recovered structures represent the global ground state crystal structures of these systems, the resulting structures may give us some insights into the condensed phase. For each considered gas-phase cluster, we generated two condensed-phase structures: 1) starting from the unoptimized gas-phase cluster; and 2) starting from the fully optimized gas-phase cluster (and indicated as "opt"). Molecular crystals were created consisting of a single NaTFSI molecule and two, three, or four NMA molecules. The resulting structures could be compared to sampling from an MD track. The structure optimizations were performed in two steps, using the PBE + D3 functional. The first step of the optimizations was aimed at quickly reducing the volume of the system and roughly positioning the different molecules in a crystal lattice. For this reason, the Brillouin zone was sampled using the Gamma point only. During the second step, the crystal volume did not vary significantly, and the local molecular geometries were optimized in detail, using the denser k-point sampling of the Brillouin zone: $3 \times 3 \times 5$ for systems with two NMA molecules and $3 \times 3 \times 3$ for systems with three or four NMA molecules. Upon convergence, the largest force on any single atom was below $2.5 \, \text{meV} \, \text{Å}^{-1}$.

[1] M. D. Slater, D. Kim, E. Lee, C. S. Johnson, *Adv. Funct. Mater.* **2013**, *23*, 947.
[2] K. Chayambuka, G. Mulder, D. L. Danilov, P. H. L. Notten, *Adv. Energy Mater.* **2018**, *8*, 1800079.
[3] L. Chen, M. Fiore, J. E. Wang, R. Ruffo, D.-K. Kim, G. Longoni, *Adv. Sustainable Syst.* **2018**, *2*, 1700153.
[4] A. Ponrouch, E. Marchante, M. Courty, J.-M. Tarascon, M. R. Palacín, *Energy Environ. Sci.* **2012**, *5*, 8572.
[5] A. Ponrouch, D. Monti, A. Boschin, B. Steen, P. Johansson, M. R. Palacín, *J. Mater. Chem. A* **2015**, *3*, 22.
[6] K. Kerman, A. Luntz, V. Viswanathan, Y.-M. Chiang, Z. Chen, *J. Electrochem. Soc.* **2017**, *164*, A1731.
[7] N. Yabuuchi, K. Kubota, M. Dahbi, S. Komaba, *Chem. Rev.* **2014**, *114*, 11636.
[8] Y. Yamada, J. Wang, S. Ko, E. Watanabe, A. Yamada, *Nat. Energy* **2019**, *4*, 269.
[9] Y. Yamada, K. Furukawa, K. Sodeyama, K. Kikuchi, M. Yaegashi, Y. Tateyama, A. Yamada, *J. Am. Chem. Soc.* **2014**, *136*, 5039.
[10] Y. Yamada, K. Usui, C. H. Chiang, K. Kikuchi, K. Furukawa, A. Yamada, *ACS Appl. Mater. Interfaces* **2014**, *6*, 10892.
[11] G. Yan, K. Reeves, D. Foix, Z. Li, C. Cometto, M. Sathiya, M. Salanne, J.-M. Tarascon, *Adv. Energy Mater.* **2019**, *9*, 1901431.
[12] G. G. Eshetu, S. Grugeon, H. Kim, S. Jeong, L. Wu, G. Gachot, S. Laruelle, M. Armand, S. Passerini, *ChemSusChem* **2016**, *9*, 462.
[13] R. Mogensen, D. Brandell, R. Younesi, *ACS Energy Lett.* **2016**, *1*, 1173.
[14] L. A. Ma, A. J. Naylor, L. Nyholm, R. Younesi, *Angew. Chem.* **2021**, *133*, 4905.
[15] O. Borodin, J. Self, K. A. Persson, C. Wang, K. Xu, *Joule* **2020**, *4*, 69.
[16] W. Liu, J. Li, W. Li, H. Xu, C. Zhang, X. Qiu, *Nat. Commun.* **2020**, *11*, 3629.
[17] Y. Jin, Y. Xu, P. M. L. Le, T. D. Vo, Q. Zhou, X. Qi, M. H. Engelhard, B. E. Matthews, H. Jia, Z. Nie, C. Niu, C. Wang, Y. Hu, H. Pan, J. G. Zhang, *ACS Energy Lett.* **2020**, *5*, 3212.
[18] K. Yoshida, M. Nakamura, Y. Kazue, N. Tachikawa, S. Tsuzuki, S. Seki, K. Dokko, M. Watanabe, *J. Am. Chem. Soc.* **2011**, *133*, 13121.
[19] E. L. Smith, A. P. Abbott, K. S. Ryder, *Chem. Rev.* **2014**, *114*, 11060.
[20] A. Boisset, S. Menne, J. Jacquemin, A. Balducci, M. Anouti, *Phys. Chem. Chem. Phys.* **2013**, *15*, 20054.
[21] J. Wang, Y. Yamada, K. Sodeyama, C. H. Chiang, Y. Tateyama, A. Yamada, *Nat. Commun.* **2016**, *7*, 1.
[22] D. E. P. Vanpoucke, P. Bultinck, I. Van Driessche, *J. Comput. Chem.* **2013**, *34*, 405.
[23] D. E. P. Vanpoucke, P. Bultinck, I. Van Driessche, *J. Comput. Chem.* **2013**, *34*, 422.
[24] D. E. P. Vanpoucke, https://github.com/DannyVanpoucke/HIVE4-tools (accessed: April 2021).
[25] J. Heyd, G. E. Scuseria, M. Ernzerhof, *J. Chem. Phys.* **2003**, *118*, 8207.
[26] K. Hendrickx, D. E. P. Vanpoucke, K. Leus, K. Lejaeghere, A. Van Yperen-De Deyne, V. Van Speybroeck, P. Van Der Voort, K. Hemelsoet, *Inorg. Chem.* **2015**, *54*, 10701.
[27] T. Miyazawa, T. Shimanouchi, S. Mizushima, *J. Chem. Phys.* **1958**, *29*, 611.
[28] D. Brouillette, D. E. Irish, N. J. Taylor, G. Perron, M. Odziemkowski, J. E. Desnoyers, *Phys. Chem. Chem. Phys.* **2002**, *4*, 6063.
[29] J. F. Vélez, M. Aparicio, J. Mosa, *Electrochim. Acta* **2016**, *213*, 831.
[30] M. Deepa, S. A. Agnihotry, D. Gupta, R. Chandra, *Electrochim. Acta* **2004**, *49*, 373.
[31] H. Vogel, *Phys. Z.* **1921**, 645.
[32] G. Tammann, W. Hesse, *Z. Anorg. Allg. Chem.* **1926**, *156*, 245.
[33] G. S. Fulcher, *J. Am. Ceram. Soc.* **1925**, *8*, 339.
[34] K. Xu, *Chem. Rev.* **2004**, *104*, 4304.
[35] K. Ueno, H. Tokuda, M. Watanabe, *Phys. Chem. Chem. Phys.* **2010**, *12*, 1648.
[36] Y. Wang, W. Chen, Q. Zhao, G. Jin, Z. Xue, Y. Wang, T. Mu, *Phys. Chem. Chem. Phys.* **2020**, *22*, 25760.
[37] A. Boisset, J. Jacquemin, M. Anouti, *Electrochim. Acta* **2013**, *102*, 120.

[38] H. G. Morrison, C. C. Sun, S. Neervannan, *Int. J. Pharm.* **2009**, *378*, 136.

[39] B. Joos, T. Vranken, W. Marchal, M. Safari, M. K. Van Bael, A. T. Hardy, *Chem. Mater.* **2018**, *30*, 655.

[40] K. Kimura, J. Hassoun, S. Panero, B. Scrosati, Y. Tominaga, *Ionics* **2015**, *21*, 895.

[41] S. Hess, M. Wohlfahrt-Mehrens, M. Wachtler, *J. Electrochem. Soc.* **2015**, *162*, A3084.

[42] B. Joos, J. Volders, R. R. da Cruz, E. Baeten, M. Safari, M. K. Van Bael, A. T. Hardy, *Chem. Mater.* **2020**, *32*, 3783.

[43] J. Wang, Y. Yamada, K. Sodeyama, E. Watanabe, K. Takada, Y. Tateyama, A. Yamada, *Nat. Energy* **2018**, *3*, 22.

[44] N. Eshraghi, S. Caes, A. Mahmoud, R. Cloots, B. Vertruyen, F. Boschini, *Electrochim. Acta* **2017**, *228*, 319.

[45] M. Bianchini, N. Brisset, F. Fauth, F. Weill, E. Elkaim, E. Suard, C. Masquelier, L. Croguennec, *Chem. Mater.* **2014**, *26*, 4238.

[46] J. Barker, R. K. B. Gover, P. Burns, A. J. Bryan, *Electrochem. Solid-State Lett.* **2006**, *9*, A190.

[47] K. Chihara, A. Kitajou, I. D. Gocheva, S. Okada, J. I. Yamaki, *J. Power Sources* **2013**, *227*, 80.

[48] M. Bianchini, F. Fauth, N. Brisset, F. Weill, E. Suard, C. Masquelier, L. Croguennec, *Chem. Mater.* **2015**, *27*, 3009.

[49] G. Yan, S. Mariyappan, G. Rousse, Q. Jacquet, M. Deschamps, R. David, B. Mirvaux, J. W. Freeland, J. M. Tarascon, *Nat. Commun.* **2019**, *10*, 1.

[50] D. De Sloovere, M. Safari, K. Elen, J. D'Haen, O. A. Drozhzhin, A. M. Abakumov, M. Šimėnas, J. Banys, J. Bekaert, B. Partoens, M. K. Van Bael, A. Hardy, *Chem. Mater.* **2018**, *30*, 8521.

[51] G. Kresse, D. Joubert, *Phys. Rev. B: Condens. Matter Mater. Phys.* **1999**, *59*, 1758.

[52] P. E. Bloechl, *Phys. Rev. B* **1994**, *50*, 17953.

[53] J. P. Perdew, K. Burke, M. Ernzerhof, *Phys. Rev. Lett.* **1996**, *77*, 3865.

[54] S. Grimme, J. Antony, S. Ehrlich, H. Krieg, *J. Chem. Phys.* **2010**, *132*, 154104.

[55] S. Grimme, S. Ehrlich, L. Goerigk, *J. Comput. Chem.* **2011**, *32*, 1456.

[56] A. D. Becke, *J. Chem. Phys.* **1988**, *88*, 2547.

[57] V. I. Lebedev, D. N. Laikov, *Dokl. Math.* **1999**, *59*, 477.

[58] V. Vasylyeva, S. K. Nayak, G. Terraneo, G. Cavallo, P. Metrangolo, G. Resnati, *CrystEngComm* **2014**, *16*, 8102.